Nanoscale Res Lett (2007) 2:476–491
DOI 10.1007/s11671-007-9095-z

NANO REVIEW

High *P–T* Nano-Mechanics of Polycrystalline Nickel

Yusheng Zhao · T. D. Shen · Jianzhong Zhang

Received: 2 August 2007 / Accepted: 4 September 2007 / Published online: 26 September 2007

Abstract We have conducted high *P–T* synchrotron X-ray and time-of-flight neutron diffraction experiments as well as indentation measurements to study equation of state, constitutive properties, and hardness of nanocrystalline and bulk nickel. Our lattice volume–pressure data present a clear evidence of elastic softening in nanocrystalline Ni as compared with the bulk nickel. We show that the enhanced overall compressibility of nanocrystalline Ni is a consequence of the higher compressibility of the surface shell of Ni nanocrystals, which supports the results of molecular dynamics simulation and a generalized model of a nanocrystal with expanded surface layer. The analytical methods we developed based on the peak-profile of diffraction data allow us to identify "micro/local" yield due to high stress concentration at the grain-to-grain contacts and "macro/bulk" yield due to deviatoric stress over the entire sample. The graphic approach of our strain/stress analyses can also reveal the corresponding yield strength, grain crushing/growth, work hardening/softening, and thermal relaxation under high *P–T* conditions, as well as the intrinsic residual/surface strains in the polycrystalline bulks. From micro-indentation measurements, we found that a low-temperature annealing ($T < 0.4\ T_m$) hardens nanocrystalline Ni, leading to an inverse Hall–Petch relationship. We explain this abnormal Hall–Petch effect in terms of impurity segregation to the grain boundaries of the nanocrystalline Ni.

Y. Zhao (✉) · J. Zhang
LANSCE-LC, Los Alamos National Laboratory, Los Alamos, NM 87545, USA
e-mail: yzhao@lanl.gov

T. D. Shen
MST-8, Los Alamos National Laboratory, Los Alamos, NM 87545, USA

Keywords Nano-mechanics · Polycrystalline nickel · High pressure and high temperature

Introduction

Nanocrystalline materials hold the promise of revolutionizing traditional materials design in many applications *via* atomic-level structural control to tailor technological properties. As opposed to the micron-scale, the nanoscale is not just another step towards miniaturization, but is a qualitatively new scale because this size constraint often produces qualitatively new behavior. It starts to become clear that when the crystal size and/or domain size become comparable with a specific physical length scale such as the mean free path, the dislocation dimension, the domain size in ferromagnets or ferroelectics, the coherence length of phonons, or the correlation length of a collective ground state like superconductivity, the corresponding physical phenomenon will be strongly affected. Extensive experimental studies over the past decade have shown that a variety of properties, such as phase stability [1], melting temperature [2], yield strength [3, 4], elastic modulus [5–8], and electronic structure [9], can strongly be altered as crystallite size decreases from micrometers to nanometers.

Nickel is a *3d* transition metal of technological importance. Nanocrystalline nickel (nano-Ni) has been the subject of considerable experimental and theoretical work in recent years. The elastic, mechanical, magnetic, and electrical properties, as well as diffusion coefficients and vibrational modes of nano-Ni have been widely studied [10–15]. In order to understand better the nano-mechanics of polycrystalline Ni, particularly its behavior under elevated pressure and/or temperature, we have recently conducted a series of synchrotron X-ray and time-of-flight

neutron diffraction experiments as well as indentation measurements to study its equation of state, constitutive properties, and hardness [4, 16–18]. To accurately characterize the unique properties of nano-Ni, we studied both nano and bulk Ni using identical techniques, and in some cases with the two metals investigated simultaneously in a single high *P–T* experiment for direct comparison. The experimental results are summarized in this review article.

Elastic Softening in Nanocrystalline Nickel Metals

Among many properties that have so far been investigated on nanocrystalline materials, the grain-size effect on the elastic properties is still a matter of controversy and has not been well understood. The Young's modulus values of nanocrystalline materials obtained in early measurements, for example, have found to be substantially lower than those of their bulk counterparts [19]. Even though this softening phenomenon can partly be attributed to the presence of a large volume fraction of pores and cracks in the as-prepared nanocrystalline materials, later measurements on porosity-free nanocrystalline samples as well as theoretical calculations [20–22] still revealed an elastic softening in materials with grain size smaller than 20 nm. Contrary to these findings, a number of recent compression studies using X-ray diffraction reported higher bulk modulus for nanocrystalline materials than for the regular polycrystals [5–8]. Furthermore, in some materials such as Fe, Ni, MgO, and CuO, the compressibility was found to be independent of the crystallite size [10, 11, 23, 24]. While there may not exist a universal law for the grain-size effect on the materials' elastic properties, it is possible that conclusions from at least some of these studies are inconclusive or perhaps misleading. The reasons can be two folds. On one hand, many of these experimental studies were focused on nanocrystalline materials only, and, therefore, the comparison with early published data for conventional materials would be vulnerable to the systematic errors of the experiments using different techniques. On the other hand, this effect may be too subtle to be resolved with the experimental methods applied. We recently studied compressibility of nano- and micro-crystalline nickel in a single high-pressure experiment using synchrotron X-ray diffraction [16]. This comparative approach would eliminate systematic errors arising from instrument response and pressure/deviatoric-stress determination and thus allows detection of small difference in compressibility measurements [25, 26].

The microcrystalline nickel powders were commercially obtained which are 99.8% pure and have a grain size distribution of 3–7 μm. The nanocrystalline powders used in this study were prepared by ball milling, starting from coarse-grained powders of Ni (<840 μm, 99.999%) supplied by Alfa Aesar (Ward Hill, Massachusetts). Five grams of powder were ball-milled for 30 h using a SPEX 8000 mill, hardened-steel vials, and 30 1-g hardened steel balls. The SEPX mill was operated inside an argon-filled glove box containing less than 1 ppm oxygen. Measurement of the Curie transition temperature by a Differential Scanning Calorimetry technique [17] suggests that the as-prepared nanocrystalline Ni contain approximately 1 at% Fe impurity. Based on the peak width analysis of X-ray diffraction at ambient conditions (see later discussion), the nanocrystalline powders have an average grain size of 12–13 nm. For both starting Ni powders, neutron diffraction at the Bragg angles of 40°, 90°, and 150° reveals no preferred orientation texture. The high-pressure X-ray diffraction experiment was performed using a cubic anvil apparatus [27] at beamline X17B2 of the National Synchrotron Light Source, Brookhaven National Laboratory. An energy-dispersive X-ray method was employed and the cell assembly used is similar to those described in the reference [26]. The two Ni samples were placed in a boron nitride sleeve, separated by a layer of NaCl, which also serves as internal pressure standard. The pressure was determined using the Decker equation of state [28] for NaCl.

The X-ray diffraction patterns at ambient pressure and 7.4 GPa (the highest pressure of the experiment) are shown in Fig. 1. Due to the surface-strain effect introduced in the process of grain-size reduction, the lattice parameters of the nanocrystalline Ni are slightly larger than those of microcrystalline Ni. In addition, the minor contamination of Fe in the nanocrystalline powders would also shift the diffraction peaks to the larger *d*-spacing [29]. Figure 1 also reveals that the diffraction peaks of nanocrystalline Ni are significantly more broaden than those of microcrystalline Ni. This is in part a result of grain-size reduction and partly caused by the enhanced density of defects (mainly dislocations produced during the heavy deformation process by ball milling) that introduce a large residual (microscopic) lattice strain.

The peak positions were determined by Gaussian peak fitting of the diffracted intensity, and the unit-cell volumes (V) were calculated by least squares fitting based on a cubic unit cell, using diffraction lines of 111, 200, 220, 311, and 222 for both nano- and micro-crystalline Ni. The relative standard deviations in the determination of lattice volumes are 0.05–0.1% for nano-crystalline Ni and 0.02–0.03% for micro-crystalline Ni. The resultant room-temperature compression data are plotted in Fig. 2, in the form of V/V_0, for a direct comparison. An inspection of Fig. 2 reveals that nanocrystalline Ni is noticeably more compressible than microcrystalline Ni. To obtain a quantitative comparison of the bulk modulus, the data of Fig. 2 are analyzed using a Eulerian finite-strain equation of state [30]. In this EOS, the pressure P is given to third order in strain f by:

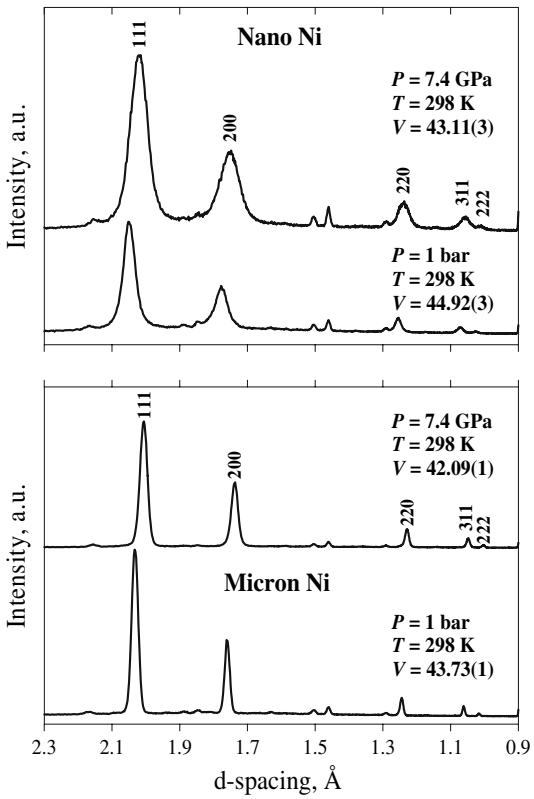

Fig. 1 X-ray diffraction patterns of nanocrystalline (upper panel) and microcrystalline Ni (lower panel) at 298 K and selected pressures. The minor peaks around *d*-spacing values of 1.3 and 1.5 Å are lead (Pb) fluorescence lines

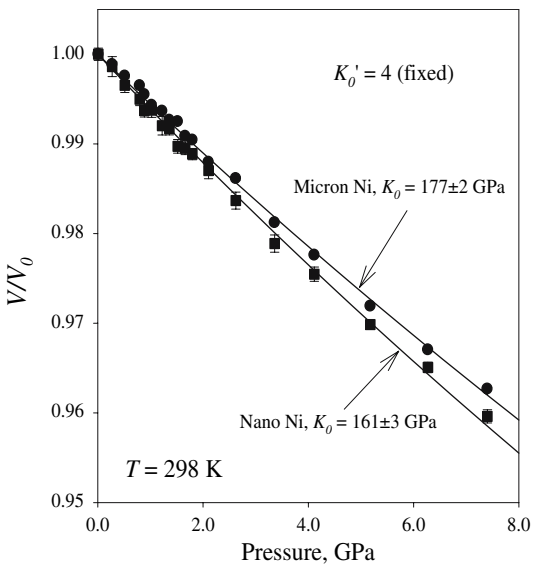

Fig. 2 Variation of the normalized unit-cell volume, V/V_0, as a function of pressure. The solid curves represent the results of least-squares fit using a second-order Eulerian finite-strain equation of state [30]. The error bars for microcrystalline Ni is smaller than the size of symbols and is hence invisible

$$P = 3f(1+2f)^{5/2} \cdot K_0[1 - 2\xi f + \ldots] \quad (1)$$

with $\xi = 3/4(4 - K_0')$ and $f = 1/2[(V/V_0)^{-2/3} - 1]$, where K_0 and K_0' are isothermal bulk modulus and its pressure derivative at ambient temperature, respectively. Because of the limited pressure range of the present study that inhibits an accurate constraint on K_0', a second-order equation of state is employed, with $\xi = 0$ in Eq. 1. The least-squares fits for the bulk modulus yield $K_0 = 161 \pm 3$ GPa for nanocrystalline Ni and $K_0 = 177 \pm 2$ GPa for microcrystalline Ni. Errors for K_0 are those of the least squares fitting; uncertainties in the measurements of pressure and unit-cell volumes were not included for error estimations. Our comparative study suggests that nanocrystalline Ni is approximately 10% more compressible than microcrystalline Ni. In addition, the bulk modulus determined for the bulk Ni is in agreement with the earlier published values (Ref. [10] and references therein).

The compressibility of nanocrystalline Ni has recently been studied by X-ray diffraction in diamond anvil cells. Chen et al. [10] measured the variation of lattice volume with pressure up to 55 GPa and found that the bulk modulus of nanocrystalline Ni ($K_0 = 185.4 \pm 10$ GPa) is similar to the value ($K_0 = 180$ GPa) previously reported for the bulk Ni. In another study of Rekhi et al. [11], the experimentally determined bulk modulus for nanocrystalline Ni ($K_0 = 228 \pm 15$ GPa) was found to be comparable to that obtained from *ab initio* calculations of their own for the bulk Ni ($K_0 = 217$ GPa). Based on these results and in contrast to the findings of the present work, both studies concluded that there is no crystallite-size effect on the compressibility of Ni. This conclusion, however, should be viewed with some caution because systematic errors typically exist among measurements with different techniques (including theoretical calculations). The comparative approach of this work can practically eliminate pressure and deviatoric stress as variables and is particularly suitable for detection of subtle difference in compressibility measurements.

The enhanced compressibility in nanocrystalline Ni is consistent with the common view of a reduced atomic density and hence a general expectation of an increasing compressibility of interatomic spacings in the surface layer of nanocrystalline materials [19, 31]. However, there is essentially no information available on the specific arrangement of atoms at the surface of nanocrystals, and so far there exist no experimental methods that can directly distinguish the compressional behavior between the surface region and the crystalline cores. Nevertheless, based on a high-pressure Mössbauer spectroscopy study [31], a technique that can discriminate between the spectral components of the intercrystalline region and the crystalline core, Trapp et al. had deduced that the surface layer of

nanocrystallie Fe has an enhanced compressibility when compared to the bulk crystalline α-Fe.

Recently, in a series of publications, Palosz and coworkers [32–34] showed that it is practically impossible to derive a single set of lattice parameters and hence a unique value of the overall bulk modulus from the positions of the Bragg reflections for nanocrystals. They proposed a methodology of the analysis of powder diffraction data for nanocrystals based on calculations of the lattice parameter values from individual Bragg reflections. Such quantities, which are associated with the specific values of the diffraction vectors Q ($Q = 2\pi/d$, where d is the d-spacing in the unit of Å) of the corresponding reflections, are termed as "*apparent lattice parameters*", *alp*. Based on theoretical calculations of powder diffraction data for nanocrystals with strained surface shell as well as experimental data of nanocrystalline SiC, the *alp* values are found to exhibit a complex dependence on Q with some characteristic minima and maxima. Careful analysis of these features may shed light on the atomic structure and behavior of nanocrystals, particularly those of the surface shell. According to Palosz's analysis, the reflections observed at very large Q could be used to probe the properties of the grain core (such as the real lattice parameter(s) of nanocrystals), whereas the reflections observed at small Q values are sensitive to the structure of the surface of the grains.

Based on the concept of *alp*, the unit-cell volumes of nano- and micro-crystalline Ni are calculated as $(alp)^3$ separately for different reflections, which are then fitted to Eq. 1. The resultant bulk moduli at the corresponding Q values are plotted in Fig. 3. For microcrystalline Ni, the bulk moduli of different reflections are identical within the mutual experimental uncertainty, thus showing no dependence on the Q values. For nanocrystalline Ni, however, the bulk moduli at $Q = 3.1$–3.5 Å^{-1} are noticeably lower ($\sim$10%) than those at $Q = 5.0$–5.9 Å^{-1}. Since the experimentally accessible Q-range is rather limited with powder X-ray diffraction, the observed range of $Q \approx 3$–6 Å^{-1} for Ni is too narrow to accurately determine the lattice parameters and hence compressibility of the grain core. A linear extrapolation of the data for nanocrystalline Ni, for example, suggests that a minimum value of $Q > 8$ Å^{-1} or an equivalent of crystallographic planes with $d < 0.78$ Å is needed to probe the grain interior of Ni nanocrystals, which should have the bulk modulus approaching that of the bulk Ni. However, with a generalized model of a nanocrystal with strained (expanded) surface layer [32–34] (see insert of Fig. 3), our observations indicate that the surface shell is 17–18% more compressible than the interior of the grain. One could also infer that the surface shell has a somewhat expanded structure with longer interatomic distances compared to the grain interior of Ni nanocrystals.

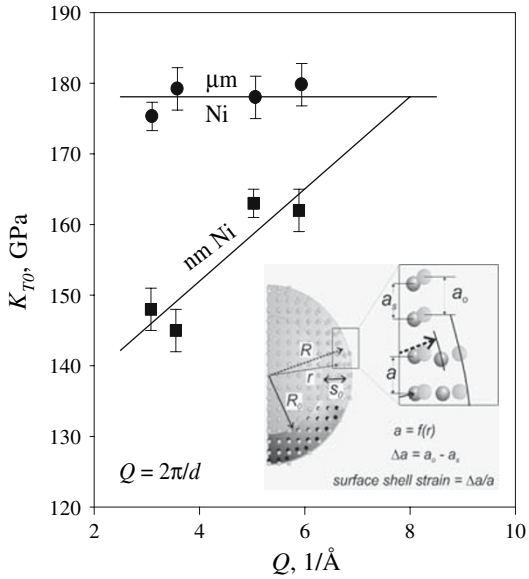

Fig. 3 The bulk moduli of nano- and micro-crystalline at the corresponding diffraction vectors Q ($Q = 2\pi/d$). The bulk modulus values plotted here are determined based on the "*apparent lattice parameters*" calculated from individual Bragg reflections. The insert at the lower right is a tentative/generalized model of a Ni nanocrystal with strained (expanded) surface layer [32–34], where R_0 is radius of the core, S_0 the thickness of the surface shell, a_0 interatomic distance in a perfect crystal lattice (in the core) and a_s interatomic distance at the grain surface

The grain-size dependence of the bulk modulus of nanocrystalline Ni has recently been investigated using molecular dynamics simulation [35]. Similar to the present findings, the calculated P–V data for Ni nanocrystals revealed a decrease of the "overall" bulk modulus up to 7% when compared with that of the single crystal Ni. Using a simple mixture model where the bulk modulus of nanocrystals is the sum of the elastic responses from two structurally different components, the bulk modulus of the surface layer at 286 K is found to be 9.2% smaller than that of the crystalline grains, which is in qualitative agreement with the present finding. Therefore, both experiment and theoretical calculation show that the enhanced "overall" compressibility of nanocrystalline Ni is a consequence of the higher compressibility of the surface shell. Our study demonstrates that careful compressional experiments with powder diffraction can be a useful means for probing the structure and behavior of the surface layer in nanocrystalline materials.

High P–T Constitutive Properties of Nano and Bulk Ni

Yield strength (σ_y) is an important constitutive property of materials to define the onset of plastic deformation and viscous flow and is conventionally determined from the

stress–strain measurements for engineering materials. Recent advancements in diffraction techniques with high intensity synchrotron X-ray and time-of-flight neutron allow the deformation studies for the bulk samples at the atomistic level [3, 4, 36–39]. Based on the classic Williamson-Hall method and its subsequent variations [40–45], the strain/strength, dislocation density, and crystal size can be derived from the peak-width analysis of diffraction data. This method will also overcome the sample porosity or impurity problems commonly faced in the conventional indentation or deformation experiments. Generally speaking, the polycrystalline diffraction profile is a convolution function of instrument response, grain size distribution, and crystal lattice deformations along the diffraction vector. During high-pressure compression experiment, the breaths of diffraction peaks broaden, and the amount of peak broadening indicates the distribution of differential strains along the diffraction vector [42], which is typically owing to different crystalline orientations relative to the loading direction and particularly to the stress concentration at grain-to-grain contacts during the powder compaction. The diffraction peak widths reach the maximum as the deviatoric stress approaches the ultimate yield strength and the sample material begins to flow plastically. By applying a stress field on crystalline sample and monitoring the peak width variation of different *hkl* diffractions as a function of pressure, one can derive the differential strain, thus the constitutive properties of the sample materials. In high-temperature annealing experiments without applied external stress, diffraction peak width sharpens with increasing temperature, reflecting the relaxation of residual strain and, in the case of nanocrystalline materials, demonstrating both the surface strain release and grain growth.

We conducted three high-pressure synchrotron X-ray diffraction experiments and two high-temperature neutron diffraction measurements on nano and bulk Ni. The Ni samples as well as the experimental methods for the X-ray diffraction experiments are the same as those described in the preceding section. Again, in all three high *P–T* X-ray diffraction experiments, the two Ni samples were studied simultaneously to allow direct and accurate comparison of materials properties between the sample pair. The time-of-flight (TOF) neutron diffraction studies at atmospheric pressure were carried out at the High-Pressure Preferred Orientation (HIPPO) beamline [46] of the Manuel Lujan, Jr. Neutron Scattering Center, Los Alamos National Laboratory. For neutron diffraction, the Ni powders were loaded into ¼-inch diameter vanadium cans, which were heated in-situ and under the vacuum. The data were collected on stepwise increases in temperatures in the range of 318–1,073 K. The acquisition time for each diffraction pattern was 2 h. Plotted in Figs. 4 and 5 are typical diffraction patters to show peak width changes under selected pressure and temperature conditions.

Following our previous work [4, 18], we express the FWHM of diffraction peaks in a length scale of angstrom (Å), Δd(FWHM), which can be used to quantify differential strain (ε) introduced by stress heterogeneity, lattice deformation, and dislocation density at high *P–T*. They can also be used to quantify the contributions of instrument response and grain sizes of polycrystalline materials, in the form of

$$\Delta d^2_{obs.}/d^2 = \left(\varepsilon^2 + \Delta d^2_{ins.}/d^2\right) + (\kappa/L)^2 \cdot d^2(P,T) \qquad (2)$$

Here, Δd_{obs} and Δd_{ins} are the observed peak width and the peak width at a stress-free state, respectively, d is the

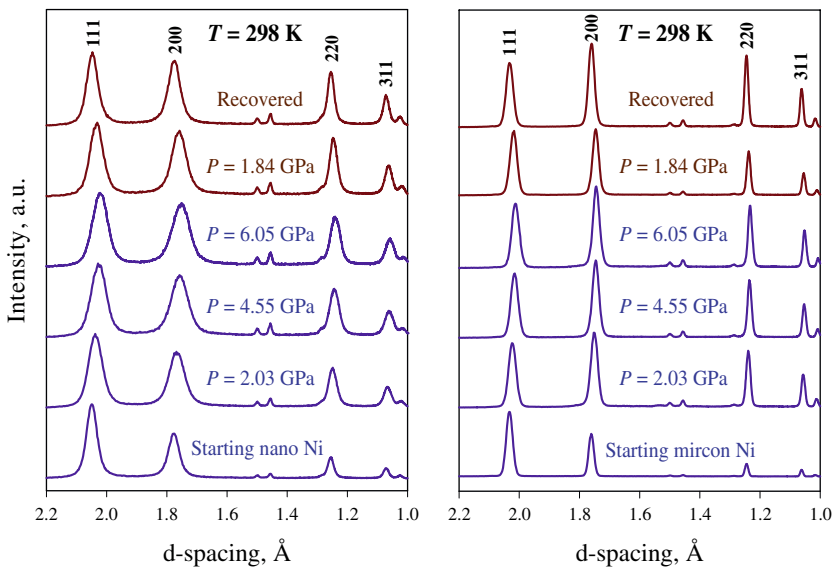

Fig. 4 Synchrotron X-ray diffraction patterns of nano (left panel) and micron Ni (right panel) at 298 K and selected pressure conditions, obtained from a single high-pressure experiment. The patterns plotted are from the experiment at pressures up to 6.05 GPa (i.e., after the bulk yielding of samples), with the blue and dark-red colors indicating compression and decompression, respectively. The peak intensities of the *hkl* diffractions are normalized relative to that of (111) at ambient conditions for width comparison purpose

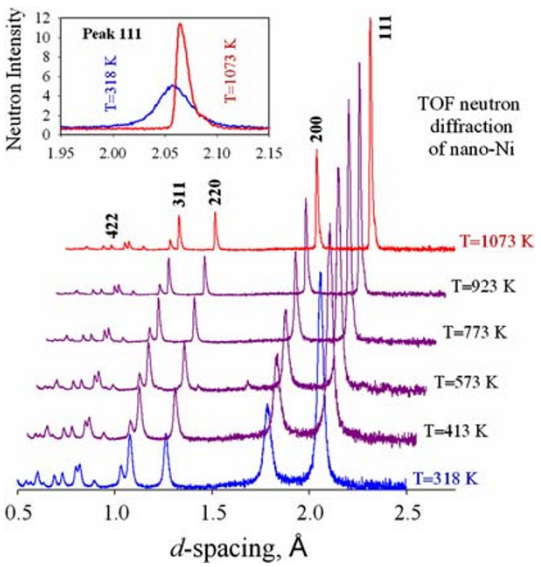

Fig. 5 The time-of-flight neutron diffraction patterns for nano Ni at atmospheric pressure and selected temperatures. The peak intensities of the *hkl* diffractions are normalized relative to that of (111) at $T = 1073$ K for width comparison purpose. The insert shows the blow-up as well as comparison of the (111) peak between $T = 318$ K and $T = 1073$ K, with vertical axis being the measured intensities

d-spacing of a given lattice plane, L the material's grain size, and κ the Scherer constant. Note that the Eq. 2 is essentially equivalent to the classic Williamson-Hall method and its subsequent variations [40–45]. With the FWHM expressed in the length unit of Å, however, Eq. 2 can be applied to any diffraction data, independent of detecting modes (energy dispersive, angular dispersive, and time-of-flight). The Eq. 2 is a typical $Y = \boldsymbol{a} + \boldsymbol{b}\cdot X$ plot. Therefore, one can derive the apparent strain $\varepsilon^2_{apparent} = \left(\varepsilon^2 + \Delta d^2_{ins.}/d^2\right)$ as well as average grain size L from the ordinate intercept and slope of the $\Delta d^2_{obs.}/d^2$ versus d^2 (P) plot, respectively. Examples of such derivation from diffraction data are illustrated in Fig. 6.

Noticeably, the observed raw data (open black circles in Fig. 6) scatter significantly and these scatterings are augmented as pressure increases. Such large data scatter is not observed in our micron-Ni sample or other micron-scale based experiments on ceramics and minerals. As a result of scattering, one cannot draw a simple straight line through the data to derive strain and grain size from the plot. In our previous studies [4, 18], we presented a correction method based on the Young's modulus for different lattice planes

$$E_{hkl} = 1 \Big/ \left(S_1 + \frac{1}{2}S_2\right) \tag{3}$$

where S_1 and S_2 are the elastic compliance data. For nano-Ni, we proposed the following normalization routings based on the square of the diffraction elasticity ratio (DER^2) and choose the least ($hkl = 111$) and/or most ($hkl = 200$) compliant planes as our references:

$$DER^2 = (E_{hkl}/E_{111})^2 \tag{4}$$

and/or

$$DER^2 = (E_{hkl}/E_{200})^2 \tag{5}$$

By multiplying the DER^2 to the observed raw data, we can correct the strain differences of individual lattice planes. As shown in Fig. 6, the corrected data (solid blue and dark cyan circles) can be readily fit to a straight line in the $\Delta d^2_{obs.}/d^2$ versus d^2 (P, T) plot and allow us to derive the apparent strain and grain size information unambiguously. From the $(E_{hkl}/E_{111})^2$ and $(E_{hkl}/E_{200})^2$ corrections, we effectively obtain the lower and upper bounds, respectively, for the apparent strains.

Loading–Unloading Loop and Energy Dissipations

In two of the synchrotron X-ray diffraction experiments we performed, the nano and bulk Ni samples were simultaneously studied at room temperature during both loading and unloading cycles. At the maximum pressures of two separate experiments (1.4 and 6.0 GPa, respectively), our results show that the absolute values of the applied strain determined using Eq. 2 for the nano-Ni are 3–4 times higher than those for the micron-Ni. To facilitate comparisons, we normalize the observed strain relative to the maximum strain at the highest pressure and the results are plotted in Fig. 7. Inspection of Fig. 7 reveals two obvious yield (kink bending) points for micron-Ni at $P_{y1} = 0.4$ GPa and $P_{y2} = 1.6$ GPa and the corresponding normalized strains at $\varepsilon^{norm.} = 0.7$ and $\varepsilon^{norm.} = 1.0$, respectively. The first one represents "micro/local" yield due to high stress concentration at the grain-to-grain contacts during the powder compactions. The second yield represents "macro/bulk" plastic deformation of entire sample, which is the true meaning of "yield" in classic mechanics.

The two-stage yielding phenomenon, however, is not as obvious in the nano-Ni, as it exhibits pronounced nonlinear ductility. The "local" plastic deformation is expected to take place at pressures much lower than 0.4 GPa, which is difficult to determine with our experimental techniques. On the other hand, the work-hardening to higher strain is clearly observed for the nano-Ni. The nano-Ni also recovers a much larger fraction of the incurred strain upon unloading, 83–84%, depending on maximum pressure, whereas the micron-Ni only recovers 49–52%, respectively. The un-recoverable strain can be caused by intergranular (e.g. elastic and plastic anisotropy) and/or intragranular (e.g. heterogeneous stress distribution and

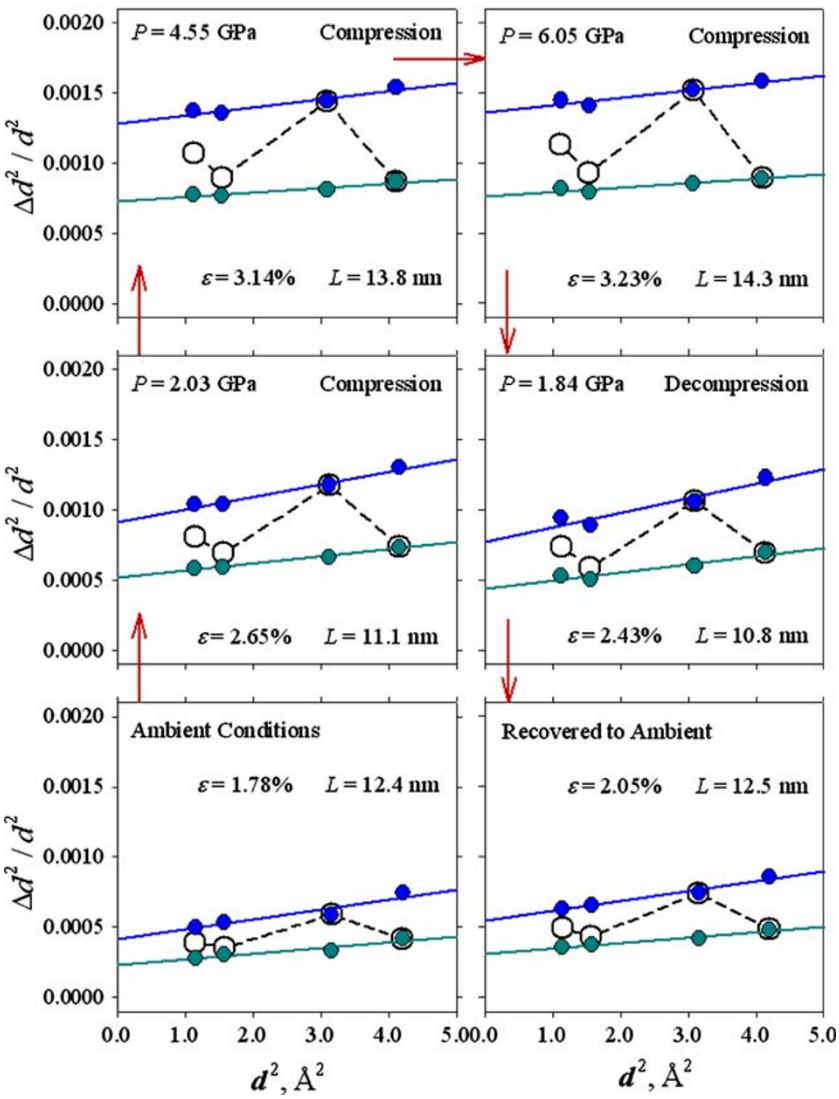

Fig. 6 The plot of $\Delta d^2_{obs.}/d^2$ versus d^2 (P, T) for X-ray diffraction data on nano-Ni. In all panels, the highly scattered raw data are shown as the open black circles. The data corrected by $DER^2 = (E_{hkl}/E_{200})^2$ and by $DER^2 = (E_{hkl}/E_{111})^2$ are shown, respectively, as solid blue and dark cyan symbols. The solid straight lines show the linear regression results of the DER^2 corrected data, with the ordinate intercept providing apparent strains and the plot slopes providing gain size information. The strains (ε) and grain sizes (L) given in all panels are the values averaged from the $(E_{hkl}/E_{200})^2$ and the $(E_{hkl}/E_{111})^2$ corrections. The red arrows indicate the experimental path. The strain (normalized) and grain size data derived for all experimental pressures are shown in Figs. 7 and 8, respectively

dislocation density) mechanisms. Previous studies [12] have shown that nano-Ni show full recovery of dislocation density when loaded in uniaxial tension. Interestingly, we observe that the recoverability for the nickel samples remain about the same level for the unloading before and/or after the bulk yielding. This, and the combination of almost full recovery for nano-Ni and less recovery for the micron-Ni in our triaxial-stress experiments, suggests that the unrecoverable part of the plastic strain in the nano-Ni is due to intergranular strains (elastic and plastic anisotropy) whereas it is mainly intragranular strain (dislocation density), in the micron-Ni.

The loading–unloading hysteresis loop illustrated in Fig. 7 is more significant for the after-yield samples (right panel) than the before-yield samples (left panel), despite the comparable recoverability for both samples. The similar strain recoverability before- and after-yields indicates that the dislocation densities in nickel samples become saturated in the elastic loading stage and there is no further development in the plastic/ductile flow stage. The much large hysteresis loop for the micron-Ni after the yield suggests that the high-P works upon the micron-Ni are dissipated as heat, as we often experienced in the fatigue failure of nail bending. The dissipation loop is much smaller for the nano-Ni sample, indicating significantly reduced energy loss in its work-hardening plasticity deformation stage. The reduced level of energy dissipation for the nano-Ni during the loading-unloading cycle indicates that the nanostructured materials may be able to more readily endure greater mechanical fatigue in cyclic load path changes, a significant discovery of nano-mechanics.

The variations of grain size with pressure on compression and decompression at room temperature are illustrated in Fig. 8 for nano-Ni. During compression (upper panel of Fig. 8), three independent experiments reveal a grain size reduction or crushing before the bulk yielding pressure (i.e., in the elastic stage of deformation

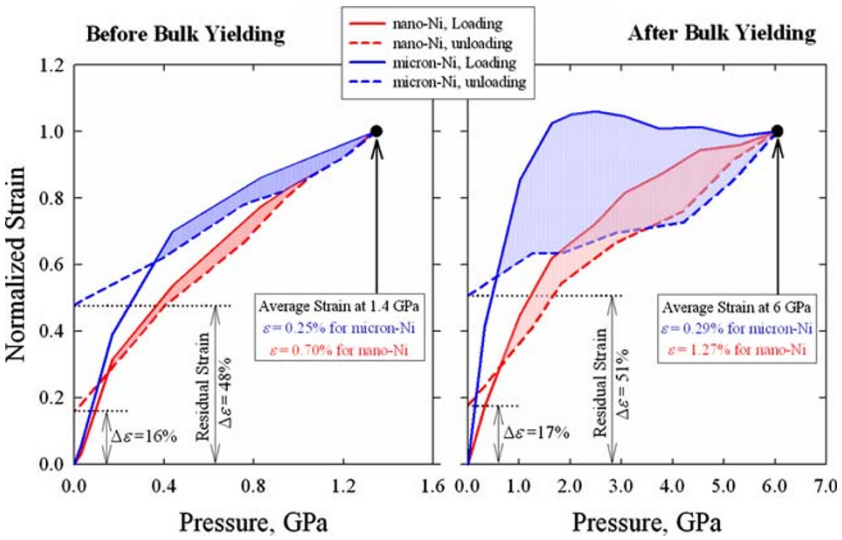

Fig. 7 The normalized applied strain $\bar{\varepsilon}_{hkl}^{ap.} = (\Delta d/d)_{hkl}/(\Delta d/d)_{hkl}^{\max .P}$ plotted as a function of pressure for nano-Ni (*red lines*) and micron-Ni (*blue lines*) during loading (*solid lines*) and unloading (*dash lines*). The left panel is for the low-pressure experiment up to 1.4 GPa (before the "macro/bulk" yield) and the right panel for the experiment at higher maximum pressure (after the "macro/bulk" yield). For both panels, the plotted lines represent the averaged strains $\bar{\varepsilon}$ derived from four different lattice planes (111, 200, 220, and 311). The average strains at the highest pressures, P_{max}, are listed in the inserted boxes. The plots illustrate two important mechanical performances: the strain recoverability ***Rec.*** = $[\bar{\varepsilon}(\max .P) - \bar{\varepsilon}(end)]/.\bar{\varepsilon}(\max .P)$ and the loading–unloading hysterisis loops, which are correlated to the high-pressure works driving energy dissipation and can reveal the degree of mechanical fatigue. The plots show clear differences between nano-Ni and micron-Ni in both mechanical qualities

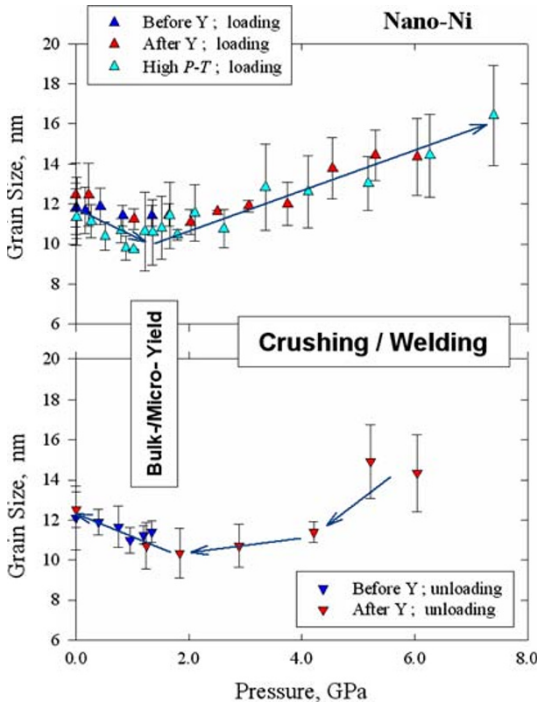

Fig. 8 The variations of grain size with pressure on compression (upper panel) and decompression (lower panel) at room temperature for nano-Ni. The blue triangles indicate the data derived from the experiment before the bulk yielding (up to 1.35 GPa) and the red triangles from the experiment after the bulk yielding (up to 6.05 GPa). The cyan triangles show the room-temperature data obtained from the high *P–T* experiment up to 7.4 GPa and 1,400 K, and therefore no grain size data can be derived from the room-temperature decompression

below ~1.8 GPa). This can be explained by the fact that high-pressure would usually suppress diffusion and enhance viscosity, as also observed in hard and brittle ceramic materials [3, 39]. After nano-Ni is plastically bulk-yielded, a quite intriguing grain growth of Ni nanocrystals at room temperature is observed, by as much as ~60% at P = 7.4 GPa. For the ductile nano-Ni metal, the observed grain growth in the plastic-yielding/viscous-flowing stage under compression is due to "cold-welding". The atomic diffusion and lattice rotation among the crystals driven by severe deviatoric stress would consume the "un-preferred" nano-grains and result in effective grain growth. Our observation agrees with Shan et al's study [13] that grain growth occurs in nano-Ni upon straining, because of nanograins' rotation during plastic deformation. Upon decompression, the variation of grain size of the samples (lower panel of Fig. 8) shows a similar but reversible trend as observed during compression, with the grain size reverting back to the starting values on fully releasing the pressure. The origin of such a reversible variation in grain size is not clearly understood but may be related to the different stress states samples experienced during decompression.

Graphic Derivation of Thermo-Mechanics

We carried out one comparative experiment using synchrotron X-rays on micron and nano Ni at simultaneously

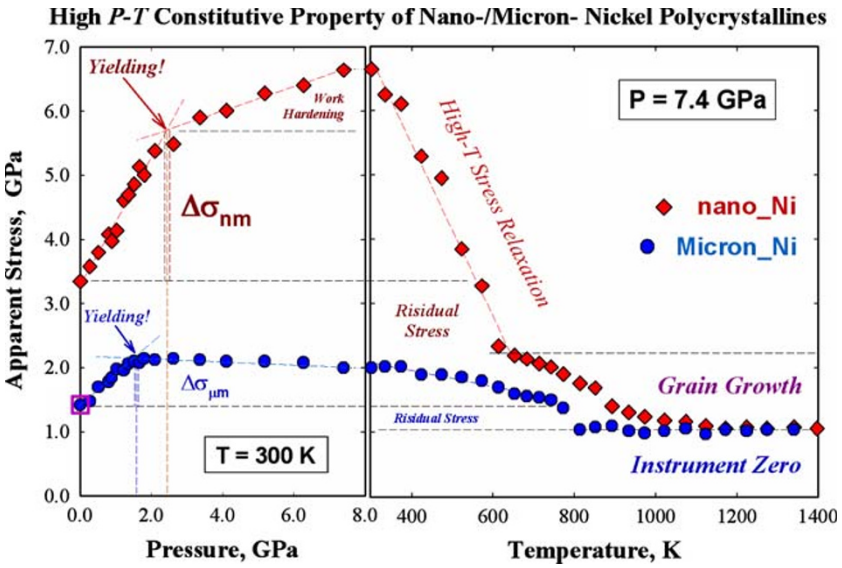

Fig. 9 Apparent stresses for nano-Ni and micron-Ni plot as functions of pressure and temperature, which include both microstrain and instrument-baseline effects. The "Yielding" points are derived by the intersections of elastic loading and plastic work-hardening/softening stages. The onset-pressures for the yielding are apparently different for the two samples. The corresponding high-*P* yield-strengths are the stress differences $\Delta\sigma$ between the yielding and the initial states. The labels of *high-T stress relaxation* and *grain growth* are simply to distinguish the dominant mechanisms at different temperature stages. The residual stresses of the samples should be read from the instrument-baseline to the initial stress states at the ambient conditions. The purple open-square symbol is to mark the recovered samples, which come back completely to the initial micron-Ni in terms of stress/strain and grain sizes. Pressure has a noticeable decrease of 0.1–0.2 GPa at high temperatures due to the cell assembly adjustments, however, the derived stress relaxations for the grain-to-grain contacts are much more significant, about 10-folds bigger for the micron-Ni and over 50-folds for the nano-Ni. The plot shows a good comparison of constitutive properties of nano-Ni and micron-Ni under high *P–T* conditions

high *P–T* conditions, up to 7.4 GPa and 1,400 K. Apparent strains have been derived using Eq. 2 and are then converted to stresses via the relationship: $\sigma = E{\cdot}\varepsilon$. Due to an observed 10% reduction in the elastic modulus derivation from our recent EOS study of nano-Ni [16] (see also Fig. 2), we used the Young's modulus of E = 180 GPa for the nano-data and E = 200 GPa for the micron-data. The pressure and temperature derivatives on the elastic modulus are still ignored; however, it should not affect the observation for the overall trend. The apparent stresses are plotted as a function of pressure and temperature in Fig. 9 to show thermo-mechanics comparisons between nano-Ni and micron-Ni. The initial difference between nano-Ni and micron-Ni is due to residual stress, surface strain, and grain size effects. As pressure increases, the grain-to-grain contact stresses enhance at a much greater rate in the nano-Ni during the elastic-plastic transition region, i.e., in the stage from "micro/local" to "macro/bulk" yielding. As the entire sample starts to loss its strength to support differential/shear stress, it is subjected to macro/bulk yield, and plastic deformation and/or viscous flow begins. Correspondingly, the diffraction peak widths do not vary as much after the bulk yield, indicating that the dislocation density in the crystalline sample reaches certain saturation.

The derived yield strength of high-*P triaxial compression* is $\Delta\sigma^{nm}_{yield} \approx 2.35$ GPa for the nano-Ni, which is similar to the uniaxial tensile strength of 2.25 GPa determined by Budrovic et al. [12]. The corresponding bulk yield strength (*compression*) of micron-Ni is $\Delta\sigma^{\mu m}_{yield} \approx 0.75$ GPa, about a factor-of-three smaller than the nano-Ni. These observations are consistent with the classic Hall–Petch law [47, 48], which indicates a significant increase in materials strength as grain size decreases to the nanometer scale. The onset-pressure for bulk yielding in micron-Ni at $P^{\mu m}_{yield} \approx 1.6$ GPa is also smaller than for the nano-Ni at $P^{nm}_{yield} \approx 2.4$ GPa, Fig. 9, Left. In the plastic stage, continuous peak broadening indicates strain hardening, whereas peak sharpening indicates strain softening under certain high *P–T* conditions. There is an evident work-hardening for the nano-Ni, where the sample can still sustain higher differential/shear stress after the yielding, and another $\Delta\sigma_{nm} \approx +1.0$ GPa is further loaded as the pressure increases to P = 7.4 GPa. However, the micron-Ni sample experiences a minor work softening at the high pressures.

It is well known that nano-metals have much less work hardening than the corresponding micron-metals in uniaxial tensile loading. Budrovic et al. [12] observed very limited strain-hardening in nano-Ni due to suppressed accumulation of dislocations after the plastic yielding. Our triaxial compression data shows opposite phenomenon, which may be because of pressure effects. It is unlikely from the artifacts due to plot of $\varepsilon_{ap.}$-vs.-P (rather than

conventional σ-vs.-ε), since the work-hardening/softening is observed in a comparative sense for the nano-/micron-samples under identical stress conditions.

As temperature increases, the stress variation in nano Ni exhibits two bending points, one at 600 K and the other near 1,000 K (Fig. 9, Right), dividing the stress-temperature variation into three different stages. Based on the grain size analysis, which will be discussed in the later part of the paper, the stress reduction at T = 300–600 K largely reflects the relaxation of both the applied/differential and surface/residual strains in the Ni nanocrystals, whereas at T = 600–1,000 K it is dominantly controlled by the grain growth. Since the stress-free state is reached at about $T > 1{,}000$ K, the initial surface/residual strains for the nano-Ni can be graphically determined as illustrated in the right panel of Fig. 9, which is 1.25×10^{-2} and in excellent with the surface strain derived from neutron diffraction data at atmospheric pressure (see later discussion). It indicates the total removal of surface strain and annealing of apparent stress of about $\Delta\sigma_{res.}^{nm} \approx -2.5$ GPa as the high-temperatures of 550 K $< T <$ 1,150 K. For micron-Ni, the relaxation of apparent stress is not as vigorous as in the nano-Ni and a stress-free state is reached at $T \geq 800$ K. Similarly, the residual stress exerted upon the starting (i.e., at ambient conditions) micron-Ni crystals can be graphically derived and is about $\Delta\sigma_{res.}^{\mu m} \approx 0.35$ GPa.

The high temperature data in the final portion of the experiment at $T > 1{,}100$ K shows a complete merging of nano-Ni and micron-Ni in terms of stress/strain levels, reconfirming the stress-free states defined in the preceding paragraph. Therefore, the corresponding apparent strain is entirely due to the instrument resolution, i.e. $\varepsilon_{ap.}^2 = \Delta d_{ins.}^2 / d^2$, and there are no contributions of strain and grain size from the samples in this stage. Our graphic approach using Eq. 2 demonstrates that the instrument contribution to the Bragg peak broadening (in the unit of Δd and further in strain and stress) can be quantified by the sample itself as long as a stress-free state is obtained through high-temperature annealing of the polycrystalline materials. The true instrument contribution is usually difficult to characterize, particularly in energy-dispersive diffraction, due to the complexities of diffraction optics and instrument calibration. In addition, the presence of residual strains and crystal defects such as dislocations in the starting powders would further complicate the de-convolution of the diffraction profiles. The Fig. 9 is a graphic de-convolution of all kinds of contributions to the apparent stress and a complete high-temperature annealing to a stress-free state provides the base line for the thermo-mechanics characterization. The graphic derivation of thermo-mechanics using Eq. 2 is important not only for a comprehensive understanding of constitutive behaviors but also for the correct application of the peak-profile analysis method.

High-T Grain Growth and Annealing of Surface Strain of Nano-Crystals

The peak positions (d) and full-widths-at-half-maximum (FWHM or Δd) of neutron diffraction data were determined by single peak fitting of the diffracted intensity using the neutron TOF peak profile function #1 of the GSAS analysis package [49]. These data were then analyzed using Eq. 2, and the results at selected temperatures are plotted in Fig. 10. As observed in X-ray diffraction, Fig. 10 shows that the degree of data scattering decreases with increasing temperature and diminishes at temperatures above 873 K. For both routines using Eqs. 4 and 5, the corrected data are lined up nicely in a linear fashion, which can be readily fit to Eq. 2 for the derivation of the surface

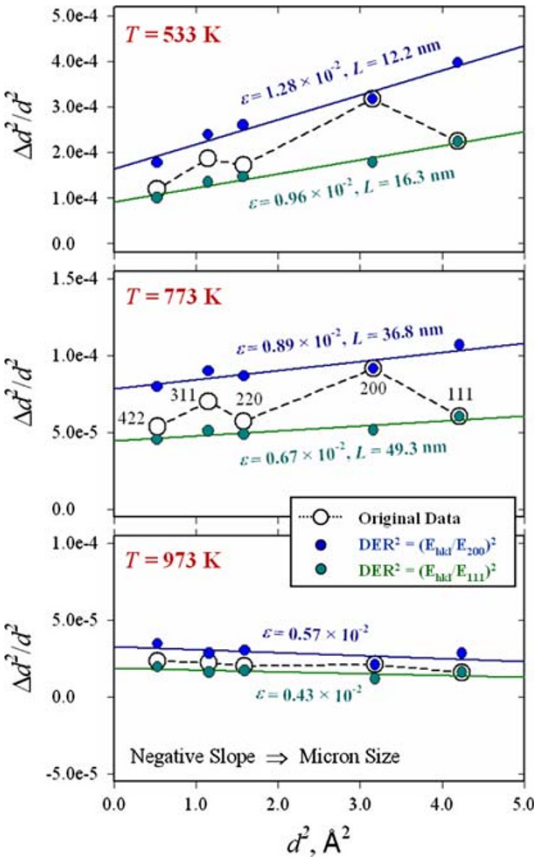

Fig. 10 The plot of $\Delta d_{obs.}^2/d^2$ versus d^2 (P, T) for neutron diffraction data on Ni. Similar to the X-ray observations (Fig. 6), the raw data below 873 K (open black symbols) are highly scattered, and the data corrected by $\mathrm{DER}^2 = (E_{hkl}/E_{200})^2$ (the solid blue symbols) are lined up nicely in a linear fashion. Also shown in the plots are corrected data using $\mathrm{DER}^2 = (E_{hkl}/E_{111})^2$, which would provide lower bounds for strains and upper bounds for grain sizes. At $T \geq 873$ K, the slopes become negative for both the raw and corrected data at $T \geq 873$ K (the bottom panel), indicating that the grain size information can no longer be extracted from Eq. 2. We interpret this phenomenon as an indication of the growth of nanocrystals approaching or into the micrometer region

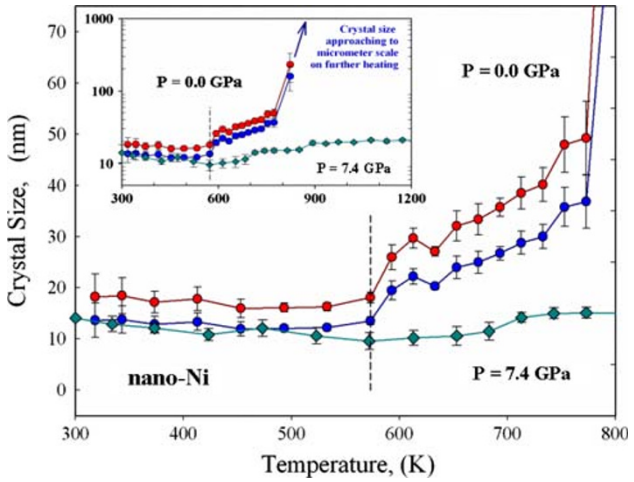

Fig. 11 Variation of grain sizes for nano Ni as a function of temperature at atmospheric pressure (neutron data) and 7.4 GPa (X-ray data). All values are derived from Eq. 2 and represent the average grain sizes for the Ni nanocrystals. For neutron data, the grain sizes derived with the $(E_{hkl}/E_{111})^2$ and $(E_{hkl}/E_{200})^2$ corrections are shown, respectively, by solid red and blue circles. The solid green diamonds denote the grain sizes derived from the high-P X-ray data using the $(E_{hkl}/E_{200})^2$ correction. The insert plots the grain size variation on a larger/logarithm scale as well as over a wider temperature range, showing the rapid growth of Ni nanocrystals approaching or entering the micrometer region. The plots clearly show that the grain growth is kinetically suppressed at high pressures

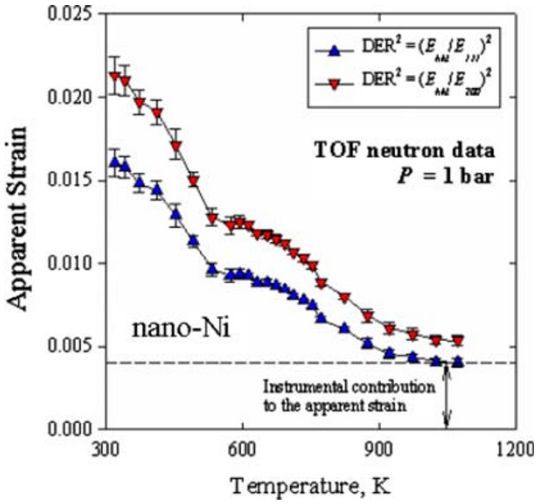

Fig. 12 Variation of the apparent strains for nano-Ni as a function of temperature at atmospheric pressure. The plotted apparent strains include both the surface strains of Ni nanocrystals and instrument contribution. The plot shows that the Ni crystals reach a stress-free state at 1,023–1,073 K, making it graphically simple to subtract the instrumental base line, which is $0.4–0.5 \times 10^{-2}$ for the DER^2 corrected data, and therefore used to determine the surface strains in Ni nanocrystals. The plot also reveals similar thermo-mechanics behaviors as observed at high pressures (Fig. 9)

strain and grain size. Fig. 10 also reveals a peculiar behavior, in the sense that the slopes become negative for both the raw and corrected data at $T \geq 873$ K (see the bottom panel) and the grain size information can no longer be extracted from Eq. 2. We consider this phenomenon as an indication of the growth of nanocrystals approaching or entering the micrometer region, therefore representing the limit of the present approach for the grain size analysis.

The grain sizes derived using Eq. 2 at all experimental temperatures are plotted in Fig. 11. The Ni nanocrystals do no show any growth at $T \leq 573$ K, whereas they grow from 13.5 to 36.8 nm with the E_{200} correction or from 18.1 to 49.3 nm with the E_{111} correction in the temperature range of 573–773 K. This growth process is accelerated at $T \geq 823$ K, with the grain size quickly approaching or entering the micrometer region. Also plotted in Fig. 11 are the grain size information derived from the high-temperature X-ray data at 7.4 GPa (i.e., the same diffraction data as used for the right panel of Fig. 9). It is clear that a similar grain growth process is observed in the lower temperature region (i.e., $T \leq 573$ K). The rate of grain growth at higher temperatures, however, is considerably smaller at 7.4 GPa than that at atmospheric pressure. These observations indicate that pressure is an effective thermodynamic parameter that controls the crystallization process. Since the grain growth is typically accompanied by long-range atomic rearrangements, it would be kinetically hindered or suppressed at high pressures. The observations of Fig. 11 support our recent conclusion that pressure is a key controlling parameters for the synthesis of nano-structured ceramic materials [50, 51].

The apparent strains derived from neutron diffraction data are plotted as a function of temperature in Fig. 12. Clearly, the thermo-mechanics behaviors of nano Ni at atmospheric pressure show the same trends as observed at 7.4 GPa (right panel of Fig. 9), with two kinks (or two bending points) on the strain-temperature curves, one at 573 K and the other at 1,023–1,073 K. Based on Fig. 12, it is evident that the strain reduction in this high temperature range is largely controlled by the grain growth. Figure 12 also reveals that a stress-free state is reached in Ni crystals at 1,023–1,073 K, making it graphically simple to quantify the instrumental strain, which is $0.4–0.5 \times 10^{-2}$ for the HIPPO neutron diffraction. This graphic approach also makes it straightforward to determine the surface strains in nano-Ni by the subtraction of these baselines of instrument contribution. At $T = 318$ K, for example, the determined surface strain is $1.20–1.6 \times 10^{-2}$, which is in good agreement with the residual strain of the nano-Ni graphically derived from the right panel of Fig. 9 (1.25×10^{-2}).

Dislocation Densities in Nanocrystalline Ni

The neutron diffraction data were also used to derive the dislocation density ρ in the nanocrystalline Ni as a function

of annealing temperature. We processed the same set of data using the method proposed by Ungar and co-workers [43–45] for comparison. The Ungar method assumes that dislocations are the main contributors to the residual/surface strain, and correspondingly, the scatter in the traditional Williamson-Hall plot or our $\Delta d^2/d^2 - d^2$ plot is attributed to the anisotropy of the dislocation strain field. In our analysis, the observed diffraction data were fitted to the following equation:

$$\left(\frac{\Delta d}{d^2}\right)^2 = \left(\frac{0.9}{L}\right)^2 + \left(\frac{\pi b^2 \rho}{2A}\right) \cdot \left(\frac{C}{d^2}\right) \quad (6)$$

where b is the modulus of the Burges vector of the dislocations, A is a constant that can be taken as 3.3 [43], and C is a contrast factor which depends on the elastic anisotropy of the material and can be characterized by the ratios of $C_{44}/(C_{11}–C_{12})$ and C_{12}/C_{44}, where C_{11}, C_{12}, and C_{44} are the elastic constants. All other parameters in Eq. 6 have the same meanings as in Eq. 2. More details on the data analysis using Eq. 6 were presented in Ref. [17].

The dislocation densities as well as grain sizes derived from Eq. 6 are shown in Fig. 13 as a function of annealing temperature. It is evident that the methods using Eqs. 2 and 6 (see Figs. 11 and 13) give rise to the comparable results for the grain size analysis, in both absolute values and their variations with temperature (e.g., the grain size is almost constant below 573 K). The dislocation density ρ in as-prepared nanocrystalline Ni powders is ~ 0.053 nm^{-2} ($=5.3 \times 10^{16}$ m^{-2}), which decreases rapidly, by a factor of ~ 3, to 0.019 nm^{-2} at 573 K. From 573 to 873 K, dislocation density continues to decrease while grain size increases with increasing temperature.

Ashby [52] suggested that the dislocations in plastically deformed crystals can be separated into "geometrically necessary" dislocations (those associated with the existence of grain boundaries, in the present case) and "statistically stored" dislocations (glissile dislocations participating in the plastic deformation). It is important to note in Fig. 13 that there is a wide annealing temperature range where the total dislocation density decreases significantly (by a factor of ~ 3) while the grain size remains approximately constant. The constancy of the grain size suggests that the density of "geometrically necessary" dislocations is not changing in this annealing temperature range and that the observed decrease in total dislocation density is due to the annihilation of the "statistically stored" dislocations that were generated by the heavy deformation of the ball milling process. At higher annealing temperatures, the grain size increases and this must correspond to a decrease in the density of geometrically necessary dislocations. Clearly, these two different types of dislocations in the Ni nanocrystals are correlated with the grain size variation. Also note that in the Ungar method the dislocation density is a parameter that characterizes the surface/residual strains caused by crystalline dislocations. Therefore, although it is not parametrically equivalent to the surface strain determined in Fig. 12, both of them describe the similar physical performances of the nanocrystals, as demonstrated by the similar trends of variation with annealing temperature in Figs. 12 and 13. As high-T annealing becomes more effective at $T > 900$ K, the surface strain approaches the instrument baseline of $\varepsilon_{ins.} = 0.005$ (Fig. 12) and the dislocation density becomes nearly zero (Fig. 13). This difference is primarily due to the fact that the Δd in Eq. 6 or Ungar approach has already subtracted instrumental contribution to the peak broadening.

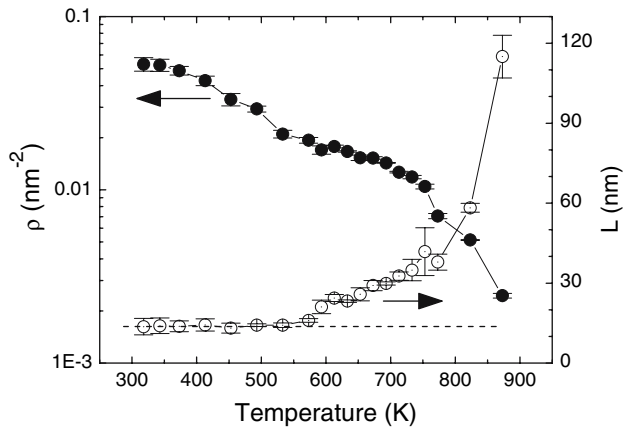

Fig. 13 Dislocation density ρ and grain size L as a function of temperature for nanocrystalline Ni. Horizontal dashed line represents the average value of L below 573 K

An Inverse Hall–Petch Effect in Nanocrystalline $Ni_{99}Fe_1$ Alloy

It is often observed that the hardness (H) of conventional coarse-grained (>1 μm) polycrystalline metals and alloys increases with decreasing grain size L according to the classic Hall–Petch relation:

$$H = H_0 + kL^{-1/2} \quad (7)$$

where H_0 and k are material constants. This Hall–Petch relation has been explained by several models, such as the pile-up of dislocations ahead of grain boundaries [47, 48], grain boundary acting as a source of dislocations [53], and the influence of grain size on the dislocation density (under the assumption that dislocation density is inversely proportional to grain size) [54, 55].

The Hall–Petch relation is fairly well obeyed in crystalline alloys with grain sizes ranging from tens of

nanometers to microns. It often fails, however, in alloys with grain sizes in the range 3–20 nm. Most nanocrystalline materials that do not obey the Hall Petch were first prepared in the smallest grain size possible (e.g. using techniques such as high-energy ball milling, electrodeposition, or gas condensation) and then were annealed (at increasingly higher temperatures) to increase their grain size. In materials prepared this way, the strength increased with increasing grain size and thus these materials were said to obey an *inverse* (or *abnormal*) Hall–Petch relationship [56–66]. The inverse Hall–Petch effect has been attributed to factors such as (i) a decrease in dislocation line tension with decreasing grain size [67]; (ii) the difficulty of generating dislocation pile-ups within grains having sizes less than a critical value [68]; (iii) a contribution to plasticity from grain-boundary diffusion creep [69–71], grain-boundary sliding [72, 73] or grain-boundary shear [74]; (iv) an overall softening with decreasing grain size due to the increase in the density of triple junctions [75, 76] or grain boundaries [77, 78]; (v) a reduced ability of the grain boundaries to obstruct the dislocation motion due to the decrease in the interfacial excess volume and energy [79]; (vi) atomic ordering near grain boundaries and triple junctions [80]; and (vii) the competition between dislocation emission (from within the grain boundaries) and grain-boundary sliding [81]. Koch and Narayan [82] reviewed the literature prior to 2001 and suggested that in several instances the observed inverse Hall–Petch effect could be due to artifacts in the nanocrystalline materials such as porosity and/or amorphous inclusions. In spite of this extensive research, the observation of an *inverse* Hall–Petch relation upon increasing the grain size of nanocrystalline materials by annealing remains poorly understood. We studied the hardness-grain size relation in nanocrystalline Ni and find inverse Hall–Petch relation. We attribute our observed inverse Hall–Petch relation to impurity (Fe) segregating to grain boundaries.

The starting nanocrystalline Ni powders were prepared using the methods described in "Elastic Softening in Nanocrystalline Nickel Metals". Following synthesis by ball milling, the powders were annealed in the same glove-box at increasing temperatures. After each 1-h anneal, the powders were rapidly cooled inside the glove box. The annealed powders were then fixed in epoxy resin. The hardened particles/epoxy-resin composites were mechanically polished using a 0.3 μm alumina paste and tested on a Micromet-4 to obtain their microhardness. Each reported microhardness value is the average of 10–20 measurements.

Figure 14 shows the microhardness (H_V) as a function of annealing temperature for nanocrystalline Ni. It is clear from Fig. 14 that the initial annealing causes a slight *increase* in the hardness. This is against what is expected

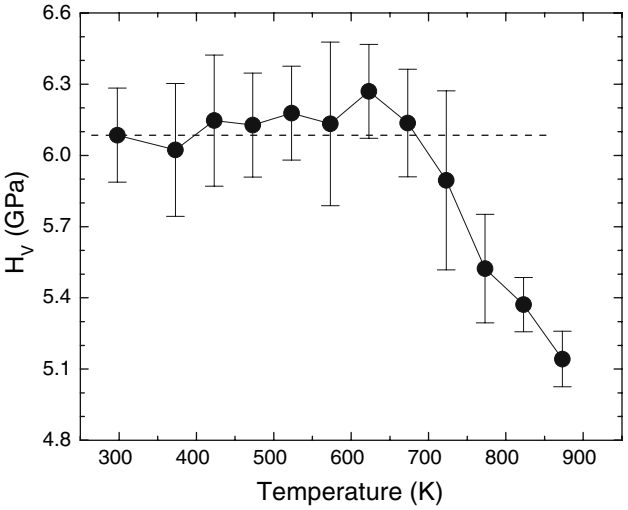

Fig. 14 Microhardness H_V as a function of annealing temperature (annealing time = 1 h) for nanocrystalline Ni. Horizontal dashed line represents the H_V value of as-prepared specimen

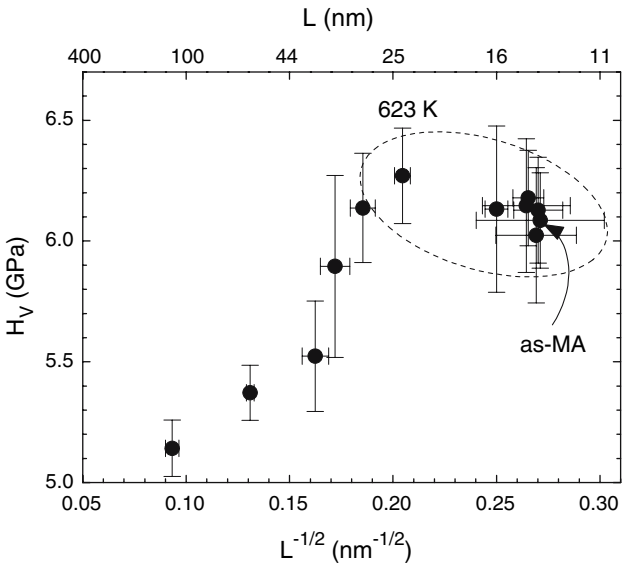

Fig. 15 Hall–Petch plot, $H_V - L^{-1/2}$, for nanocrystalline Ni whose grain size was increased by isochronal annealing. Dashed oval denotes the regime where data follows an *inverse* Hall-Petch relation

since annealing usually *decreases* the hardness of materials. Figure 15 shows a Hall–Petch plot (H_V as a function of $L^{-1/2}$) for nanocrystalline Ni. For the grain size larger than 25 nm, the variation of H_V follows a classic Hall–Petch relation. Below 25 nm, the data reveals an *inverse* Hall–Petch relationship, as identified by the dashed oval in Fig. 15.

Since the inverse Hall–Petch relationship is observed in our nanocrystalline Ni (containing ~1 at% Fe) but not in ultra-pure nanocrystalline Fe, studied using the same experimental methods [17], it is not unreasonable to

assume that the inverse Hall–Petch relationship observed upon annealing nanocrystalline Ni is apparently due to the segregation of solutes to grain boundaries. Two previous studies on ball milled Fe seem to confirm our conclusions. Malow and Koch [83] ball-milled 99.9% pure Fe to achieve an initial grain size of ~13 nm. This powder was sequentially annealed and the hardness was measured as a function of grain size. Here the Hardness versus $L^{-1/2}$ followed a normal Hall–Petch relation. This contrasts with the experiments of Kahn et al. [65] who started with 98.5% pure Fe (the type of impurities were not specified) and added stearic acid [$CH_3(CH_2)_{16}CO_2H$] to the milling vial to minimize the agglomeration of the powder during ball milling. This additive most likely introduced additional impurities in the nanocrystalline product. The grain size of the as-prepared powder was 16 nm. Increasing the grain size to 23 nm (by annealing) caused the hardness to *increase* by 27%, in violation of the Hall–Petch relation [65]. Then, a further increase in grain size (by annealing at higher temperatures) caused the hardness to decrease, in agreement with the Hall–Petch relation.

Several mechanisms may contribute concurrently to the plastic deformation of nanocrystalline materials (grain-boundary sliding, grain-boundary rotation, and the generation of dislocations at grain-boundaries) [84]. All of these may be affected by the segregated solutes. Segregation of solutes and impurities in grain boundary may lead to three effects: (1) lowering the grain boundary energy, enabling the formation of low-energy grain boundary, (2) lowering the grain boundary free volume and thus the grain boundary diffusion coefficient, and (3) decreasing the stress gradient in the grain boundary regions. All of these three effects may increase the resistance for grain-boundary sliding, grain-boundary rotation, and the generation of dislocations at grain-boundaries. This reveals increased hardness of in annealed nanocrystalline materials.

Hardness increase induced by annealing has also been also frequently observed in plastically deformed large-grained polycrystalline materials. This phenomenon has been named as a "strain-ageing hardening" effect which means annealing (ageing) the deformed materials leads to hardening. In $Fe_{97}Si_3$ alloy (grain size = 30 μm) that was plastically deformed to ~20% strain, annealing at 573 K for an hour increases the hardness by ~4.6% [52]. Origin of this increased hardness, however, is different than that in our nanocrystalline Ni. In plastically deformed large-grained polycrystalline materials, the major resistance for further plastic deformation comes from the long-range stress field of multiplicated dislocations. Annealing can segregate Si to the multiplicated dislocations, increasing the stress that is needed to move these dislocations.

Summary

We have conducted high *P–T* synchrotron X-ray and time-of-flight neutron diffraction experiments as well as indentation measurements to study equation of state, constitutive properties, and hardness on nanocrystalline and bulk nickel. Our results present a clear evidence of elastic softening in nanocrystalline Ni as compared with the bulk nickel. It is also observed that the bulk moduli determined using the "*apparent lattice parameters*" are 17–18% lower at the smaller diffraction vectors ($Q = 2\pi/d$) than those at the larger Q values. These findings support the results of molecular dynamics simulation and a generalized model of a nanocrystal with expanded surface layer. Based on the peak-profile analysis of diffraction data, the yield strength for nano-Ni is determined to be 2.35 GPa, more than three times higher than that of bulk Ni. Contrary to tensile experiments of uniaxial loading, we observe significant work-hardening for the nano-Ni in high-pressure plastic deformation stage, whereas the micron-Ni experiences minor high-pressure work-softening and considerable energy dissipation into heat. The significantly reduced energy dissipation for the nano-Ni during the loading-unloading cycle indicates that the nanostructured materials can endure much greater mechanical fatigue in cyclic loadings. Nano-Ni exhibits grain crushing in the elastic stage of deformation but steady grain growth during bulk plastic deformation under high-pressure loading. During the high-temperature annealing, Ni nanocrystals show drastic stress reduction with increasing temperature and grain growth above 573 K. The rate of grain growth at high temperature, however, is considerably smaller at 7.4 GPa than that at atmospheric pressure, indicating that pressure is an effective thermodynamic parameter for controlling the crystallization process. From micro-indentation measurements, our analysis suggests that the inverse Hall–Petch effect observed in the annealed nanocrystalline Ni of different grain size can be ascribed to the impurity effects. Annealing allows impurity Fe to migrate to the grain boundaries, increasing the stress needed to initiate grain-boundary mediated plastic deformation in nanocrystalline Ni.

Acknowledgements Los Alamos National Laboratory is operated by Los Alamos National Security LLC under DOE contract DE-AC52-06NA25396. This work has benefited from the use of the Lujan Neutron Scattering Center at LANSCE, which is funded by the U.S. Department of Energy's Office of Basic Energy Sciences. This work was also supported by the Laboratory Directed Research & Development (LDRD) program of the Los Alamos National Laboratory. The high *P–T* X-ray diffraction experiments were carried out at the beamlines X17B2 of National Synchrotron Light Source, Brookhaven National Laboratory, which is supported by the Consortium for Materials Properties Research in Earth Sciences (COMPRES) under NSF Cooperative Agreement EAR 01-35554.

References

1. C.C. Chen, A.B. Herhold, C.S. Johnson, A.P. Alivisatos, Science **276**, 398 (1997)
2. A.N. Goldstein, C.M. Echer, A.P. Alivisatos, Science **256**, 1425 (1992)
3. J. Chen, N. Schmidt, J.H. Chen, J. Zhang, L. Wang, D.J. Weidner, J. Mat. Sci. **40**, 5763 (2005)
4. Y. Zhao, J. Zhang, B. Clausen, T.D. Shen, G.T. Gray, L. Wang, Nano Lett. **7**, 426 (2007)
5. S.H. Tolbert, A.P. Alivisatos, Annu. Rev. Phys. Chem. **46**, 595 (1995)
6. Z. Wang, Y. Zhao, D. Schiferl, C. Zha, R. Downs, T. Sekine, Appl. Phys. Lett. **83**, 3174 (2003)
7. Z. Wang, Y. Zhao, D. Schiferl, C. Zha, R. Downs, Appl. Phys. Lett. **85**, 124 (2004)
8. J.Z. Jiang, J.S. Olsen, L. Gerward, S. Morup, Europhys. Lett. **44**, 620 (1998)
9. T. Van Buuren, L.N. Dinh, L.L. Chase, W.J. Siekhaus, L.J. Terminello, Phys. Rev. Lett. **80**, 3803 (1998)
10. B. Chen, D. Penwell, M.B. Kruger, Solid State Comm. **115**, 191 (2000)
11. S. Rekhi, S.K. Saxena, R. Ahuja, B. Johansson, J. Hu, J. Mat. Sci. **36**, 4719 (2001)
12. Z. Budrovic, H. Van Swygenhoven, P.M. Derlet, S. Van Petegem, B. Schmitt, Science **304**, 273 (2004)
13. Z.W. Shan, E.A. Stach, J.M.K. Wiezorek, J.A. Knapp, D.M. Follstaedt, S.X. Mao, Science **305**, 654 (2004)
14. E. Bonetti, E.G. Campari, L. Pasquini, et al., J. Appl. Phys. **84**, 4219 (1998)
15. R.Z. Valiev, G.F. Korznikova, K.Y. Mulyukov, et al., Philos. Mag. B **75**, 803 (1997)
16. J. Zhang, Y. Zhao, B. Palosz, Appl. Phys. Lett. **90**, 043112 (2007)
17. T.D. Shen, R.B. Schwarz, S. Feng, J.G. Swadener, J.Y. Huang, M. Tang, Jianzhong Zhang, S.C. Vogel, Yusheng Zhao, Acta Mater. **55**, 5007 (2007)
18. Y. Zhao, J. Zhang, submitted to Int. J. Plast. (2007)
19. H. Gleiter, Prog. Mat. Sci. **33**, 223 (1989)
20. T.D. Shen, C.C. Koch, T.Y. Tsui, G.M. Pharr, J. Mater. Res. **10**, 2892 (1995)
21. J.A. Lupo, M.J. Sabochick, Nanostruct. Mater. **1**, 131 (1992)
22. A. Latapie, D. Farkas, Scripta Mater. **48**, 611 (2003)
23. B. Chen, D. Penwell, M.B. Kruger, A.F. Yue, B.J. Fultz, Appl. Phys. **89**, 4794 (2001)
24. Z.W. Wang, V. Pischedda, S.K. Saxena, P. Lazor, Solid State Commun. **121**, 275 (2002)
25. R.M. Hazen, Science **159**, 206 (1993)
26. J. Zhang, P. Kostak, Phys. Earth Planet. Int. **129**, 301 (2002)
27. D.J. Weidner, M.T. Vaughan, J. Ko, Y. Wang, X. Liu, A. Yeganehhaeri, R.E. Pacalo, Y. Zhao, in *High-Pressure Research: Application to Earth and Planetary Sciences*, vol 67, ed. by Y. Syono, M.H. Manghnani (AGU, Washington DC, 1992), pp. 13–17
28. D.L. Decker, J. Appl. Phys. **42**, 3239 (1971)
29. L.W. McKeehan, Phys. Rev. **21**, 402 (1923)
30. F. Birch, J. Geophys. Res. **83**, 1257 (1978)
31. S. Trapp, C.T. Limbach, U. Gonser, S.J. Campbell, H. Gleiter, Phys. Rev. Lett. **75**, 3761 (1995)
32. B. Palosz, S. Stel'makh, E. Grzanka, S. Gierlotka, R. Pielaszek, U. Bismayer, S. Werner, W. Palosz, J. Phys. Condens. Matter. **15**, 1 (2003)
33. B. Palosz, S. Stel'makh, E. Grzanka, S. Gierlotka, Y. Zhao, W. Palosz, Mat. Res. Soc. Symp. Proc. **778**, 29 (2003)
34. B. Palosz, E. Grzanka, S. Gierlotka, S. Stel'makh, R. Pielaszek, U. Bismayer, J. Neuefeind, H.P. Weber, T. Proffen, R. Von Dreele, W. Palosz, Z. Kristallogr. **217**, 497 (2002)
35. S.J. Zhao, K. Albe, H. Hahn, Scripta Mater. **55**, 473 (2006)
36. D.J. Weidner, Y. Wang, M.T. Vaughan, Science **266**, 419 (1994)
37. J. Zhang, L. Wang, D.J. Weidner, T. Ucchida, J. Xu, Am. Mineral. **87**, 1005 (2002)
38. D.W. Brown, M.A.M. Bourke, B. Clausen, T.M. Holden, C.N. Tome, R.A. Varma, Metall. Mater. Trans. A **34A**, 1439 (2003)
39. J. Qian, C. Pantea, J. Zhang, Y. Zhao, Y. Wang, T. Uchida, J. Am. Ceramic Soc. **88**, 903 (2005)
40. G.K. Williamson, W.H. Hall, Acta Metall. **1**, 22 (1953)
41. L. Gerward, S. Morup, H. Topsoe, J. Appl. Phys. **47**, 822 (1976)
42. D.J. Weidner, Y. Wang, M.T. Vaughan, Geophys. Res. Lett. **21**, 753 (1994)
43. A. Revesz, T. Ungar, A. Borbely, J. Lendvai, Nanostruct. Mater. **7**, 779 (1996)
44. T. Ungar, G. Tichy, Phys Status Solidi A **171**, 425 (1999)
45. T. Ungar, I. Dragomir, A. Revesz, A. Borbely, J Appl Crystallogr **32**, 992 (1999)
46. H.R. Wenk, L. Lutterotti, S. Vogel, Nucl. Instrum. Methods A **515**, 575 (2003)
47. E.O. Hall, Proc. Phys. Soc. **B64**, 747 (1951)
48. N.J. Petch, J. Iron Steel Inst. **174**, 25 (1953)
49. A.C. Larson, R.B. Von Dreele, Los Alamos National Laboratory Report LAUR 86–748 (2004)
50. Y. Zhao, D. He, L.L. Daemen, J. Huang, T.D. Shen, R.B. Schwarz, Y. Zhu, D.L. Bish, J. Zhang, G. Shen, Z. Liu, J. Qian, T.W. Zerda, J. Mat. Res. **17**, 3139 (2002)
51. Y. Zhao, J. Qian, L.L. Daemen, C. Pantea, J. Zhang, G. Voronin, T.W. Zerda, Appl. Phys. Lett. **84**, 1356 (2004)
52. M.F. Ashby, Philos. Mag. **21**, 399 (1970)
53. J.C.M. Li, Trans. AIME **227**, 239 (1963)
54. H. Conrad, in *Electron Microscopy and Strength of Crystals*, ed. by G. Thomas, J. Washburn (Interscience, New York, 1963), p. 299
55. A.W. Thompson, M.I. Baskes, W.F. Flanagan, Acta Metall. **21**, 1017 (1973)
56. A.H. Chokshi, A. Rosen, J. Karch, H. Gleiter, Scripta Metall. **23**, 1679 (1989)
57. K. Lu, W.D. Wei, J.T. Wang, Scripta Metall. Mater. **24**, 2319 (1990)
58. T. Christman, M. Jain, Scripta Metall. Mater. **25**, 767 (1991)
59. D.K. Kim, K. Okazaki, Mater. Sci. Forum **88–90**, 553 (1992)
60. H. Chang, C.J. Altstetter, R.S. Averback, J. Mater. Res. **7**, 2962 (1992)
61. X.D. Liu, J.T. Wang, Z.Q. Hu, B.Z. Ding, Mater. Sci. Eng. **A169**, L17 (1993)
62. H. Alves, M. Ferreira, U. Köster, B. Müller, Mater. Sci. Forum **225–227**, 769 (1996)
63. T. Volpp, E. Göring, W.M. Kuschke, E. Artz, Nanostruct. Mater. **8**, 855 (1997)
64. A.S. Kahn, H. Zhang, L. Takacs, Int. J. Plastic. **16**, 1459 (2000)
65. S. Guicciardi, D. Sciti, C. Melandri, A. Bellosi, J. Am. Ceram. Soc. **87**, 2101 (2004)
66. A. Bellosi, J. Vicens, V. Medri, S. Guicciardi, Appl. Phys. A **81**, 1045 (2005)
67. R.O. Scattergood, C.C. Koch, Scripta Metall. Mater. **27**, 1195 (1992)
68. T.G. Nieh, J. Wadsworth, Scripta Metall. Mater. **25**, 955 (1991)
69. R.A. Masumura, P.M. Hazzledine, C.S. Pande, Acta Mater. **46**, 4527 (1998)
70. V. Yamakov, D. Wolf, S.H. Phillpot, H. Gleiter, Acta Mater. **50**, 61 (2002)
71. H.S. Kim, Y. Estrin, Acta Mater. **53**, 765 (2006)
72. H. Hahn, P. Mondal, K.A. Padmanabhan, Nanostruct. Mater. **9**, 603 (1997)
73. J. Schiotz, T. Vegge, F.D. Di Tolla, K.W. Jacobsen, Phys. Rev. B **60**, 11971 (1999)

74. H. Conrad, J. Narayan, Scripta Mater. **42**, 1025 (2000)
75. G. Palumbo, U. Erb, K.T. Aust, Scripta Metall. Mater. **24**, 2347 (1990)
76. Q. Xiang, X.M. Guo, Int. J. Solids Struct. **43**, 7793 (2006)
77. J.E. Carsley, J. Ning, W.W. Milligan, S.A. Hackney, E.C. Aifantis, Nanostruct. Mater. **5**, 441 (1995)
78. G.J. Fan, H. Choo, P.K. Liaw, E.J. Lavernia, Mater. Sci. Eng. **A409**, 243 (2005)
79. K. Lu, M.L. Sui, Scripta Metall. Mater. **28**, 1465 (1993)
80. A. Hasnaoui, H. Van Swygenhoven, P.M. Derlet, Acta Mater. **50**, 3927 (2002)
81. D. Farkas, W.A. Curtin, Mater. Sci. Eng. **A412**, 316 (2005)
82. C.C. Koch, J. Narayan, Mat. Res. Soc. Symp. Proc. **634**, B5.1.1 (2001)
83. T.R. Malow, C.C. Koch, Metall. Mater. Trans. **A29**, 2285 (1998)
84. M.A. Meyers, A. Mishra, D.J. Benson, Prog. Mater. Sci. **51**, 427 (2006)